StainedSweeper: Compact, Variable-Intensity Light-Attenuation Display with Sweeping Tunable Retarders

Yuichi Hiroi *

Cluster Metaverse Lab

Takefumi Hiraki †

Cluster Metaverse Lab
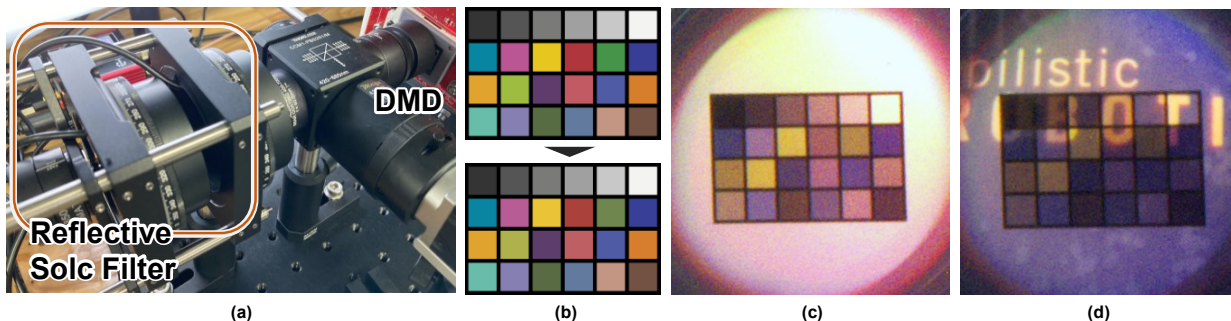
Yuta Itoh ‡

The University of Tokyo

Fig. 1. (a) Proof-of-concept prototype of our StainedSweeper system. Our system modulates the color and brightness of the incident light pixel by pixel with a single SLM by synchronously controlling the DMD and the polarized color filter, a reflective Solc filter. (b) Top: An example of a target image (Macbeth color chart), bottom: reproduced image based on DMD control optimization. The DMD time-multiplexing matrix is optimized on the basis of the color filter characteristics measured by the system. (c) Viewpoint image. A white surface light source is used as the background. (d) Viewpoint image when a real object is placed in the background. It can be seen that our system can display a subtractive image in the see-through view.

Abstract—Light Attenuation Displays (LADs) are a type of Optical See-Through Head-Mounted Display (OST-HMD) that present images by attenuating incoming light with a pixel-wise polarizing color filter. Although LADs can display images in bright environments, there is a trade-off between the number of Spatial Light Modulators (SLMs) and the color gamut and contrast that can be expressed, making it difficult to achieve both high-fidelity image display and a small form factor. To address this problem, we propose StainedSweeper, a LAD that achieves both the wide color gamut and the variable intensity with a single SLM. Our system synchronously controls a pixel-wise Digital Micromirror Device (DMD) and a nonpixel polarizing color filter to pass light when each pixel is the desired color. By sweeping this control at high speed, the human eye perceives images in a time-multiplexed, integrated manner. To achieve this, we develop the OST-HMD design using a reflective Solc filter as a polarized color filter and a color reproduction algorithm based on the optimization of the time-multiplexing matrix for the selected primary color filters. Our proof-of-concept prototype showed that our single SLM design can produce subtractive images with variable contrast and a wider color gamut than conventional LADs.

Index Terms—Light attenuation display, see-through display, augmented reality, time-multiplexing, polarized color filter

---◆---

1 INTRODUCTION

Optical See-Through Head-Mounted Displays (OST-HMDs) overlay digital information in the wearer's field of view while providing a direct view of the real scene. OST-HMDs play a key role in Augmented Reality (AR) experiences by seamlessly blending digital and real space [16].

Typical OST-HMDs additively superimpose light from the display onto the wearer's view of the real scene using optical elements such as beam combiners. As a result, OST-HMDs cannot occlude light from the real scene, leading to challenges with an inherently narrow dynamic range [5, 37]. For example, when using OST-HMDs in brightly lit outdoor environments, the virtual images may become barely visible.

To improve the dynamic range of OST-HMDs, occlusion-capable OST-HMDs (OCOST-HMDs) [22] integrate occlusion masks into OST-HMDs to block light from the real scene. A Spatial Light Modulator (SLM), such as a Digital Micromirror Device (DMD) or Liquid Crystal (LC) on Silicon, is used as an occlusion mask to control the brightness

*e-mail: y.hiroi@cluster.mu

†e-mail: t.hiraki@cluster.mu

‡e-mail: yuta.itoh@iii.u-tokyo.ac.jp

• *Yuichi Hiroi and Takefumi Hiraki is with Cluster Metaverse Lab., E-mail: y.hiroi, t.hiraki@cluster.mu. Yuta Itoh is with The University of Tokyo, E-mail: yuta.itoh@iii.u-tokyo.ac.jp.*

of incident light on a pixel-wise basis.

However, OCOST-HMDs cannot yet fully resolve the dynamic range issue in bright environments. First, the occlusion layer cannot completely block the incoming light. Secondly, the display must be brighter, resulting in inefficient power consumption.

As an emerging approach to fully solve these brightness issues, Light Attenuation Displays (LADs) [15] propose a new OST-HMD paradigm that uses SLMs as pixel-wise color filters to attenuate incoming light and display color images. In LAD, a pixel-wise color filter is realized by sandwiching two orthogonal polarizers to a Phase-Only Spatial Light Modulator (PSLM). Figure 2 shows a comparison of the existing design of LADs. Although the early LAD [15] (Fig. 2 a) was realized with a single PSLM polarizing color filter, the wide bandwidth of the color filter limited the color gamut. Additionally, this early LAD does not control the intensity. If intensity were to be controlled, an additional occlusion mask would be required (Fig. 2 b). StainedView [19] (Fig. 2 c) improved LAD by cascading two PSLMs to narrow the color filter bandwidth and cascading a DMD for intensity control. However, this design requires three SLMs, making it difficult to achieve a wearable form factor. Therefore, no LAD method could control a wide color gamut and brightness while maintaining the configuration of a single SLM.

In this paper, we propose StainedSweeper, a wide-gamut, intensity-variable LAD with a single SLM (Fig. 2 d). Figure 3 illustrates the
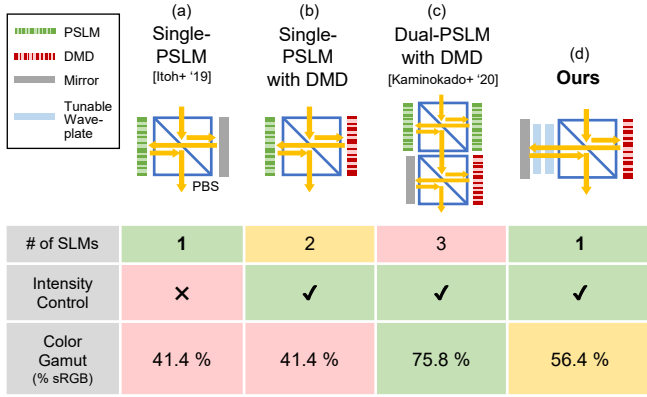
Fig. 2. Comparison of our system with existing LADs. From top to bottom rows: simplified optical design, number of SLMs, availability of intensity control, and the ratio of gamut to sRGB in the CIE 1931 xy chromaticity diagram. (a) The first LAD with a single PSLM [15]. (b) The variable intensity design that combines a PSLM with a DMD. (c) LAD designed to improve color gamut by cascading PSLM [19]. (d) Our design with tunable waveplates and DMD.

Fig. 3. Our StainedSweeper concept. The system controls a uniform tunable color to display multiple primary colors c_i, then synchronizes each pixel of the DMD to it. The duration t_i of each primary color is distributed unevenly based on optimization. In addition, the open/close ratio of each pixel of the DMD (i.e., the intensity of each primary color) is also optimized to reproduce the target color. By completing this schedule below CCFF (40 ms), the human eye perceives the integrated color image.

concept of our StainedSweepersystem. Our system synchronizes a DMD and a uniform (not pixel-wise) color filter using tunable waveplates that switch its phase retardance with a very fast response to the input voltage. Our system sweeps the retardance of the tunable waveplates at a very high speed and synchronously controls the DMD to pass light when each pixel is in the desired color. By performing this control within the critical color fusion frequency (CCFF) of the human eye ($\geq$ 25 Hz) [17], the system enables the human eye to perceive the image in an integrated manner.

To realize StainedSweeper, this paper proposes a see-through optical design using a reflective Solc filter and an optimization for the time-multiplexing control of the DMD to reproduce the desired color. The reflective Solc filter uses waveplates that are alternately rotated by the same angle, allowing the system to be smaller and the color filter to have a narrower bandwidth. Using this filter, we first calculate the color filter characteristics of our LAD design and determine primary colors for time-multiplexing that supports a wide color gamut. Then, we propose to optimize the time-multiplexing matrix used to reproduce the target color using the primary colors. Finally, we implemented a proof-of-concept prototype to reproduce color images by controlling the DMD and waveplates according to an optimized time-multiplexing matrix.

Our primary contributions are that we:

- Introduce StainedSweeper, a variable-intensity, wide-gamut LAD with a single SLM by synchronously controlling a tunable Solc filter and DMD.

- Develop a see-through optical design using a reflective Solc filter and a color reproduction algorithm based on optimizing the time-multiplexing matrix for the primary color.

- Implement a proof-of-concept prototype that displays color images in bright environments.

- Discuss the differences in color filter properties between simulations and prototypes and provide future research directions.

2 RELATED WORK

2.1 OCOST-HMDs and LADs

Our system is based on an optical design concept in the field of OCOST-HMDs that improves the dynamic range of OST-HMDs by occluding light from the real world environment. A typical OCOST-HMD uses SLMs that modulate the intensity of incident light, such as a transmissive LCD [3, 22, 32, 36], reflective LCoS [6, 7, 47, 48], or DMD [21, 25, 43], to create a black occlusion mask.
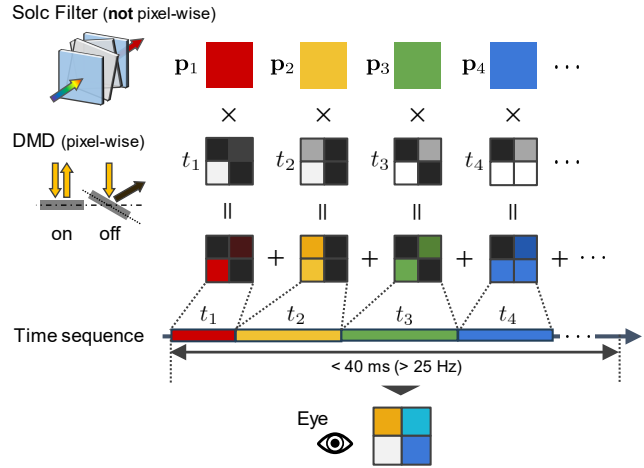
The simplest approach to implement OCOST-HMD is to place the occlusion mask directly between the OST-HMD and the eye [31, 32]. This approach allows for a smaller form factor and has been introduced in commercial OST HMDs such as Magic Leap 2. In this case, the incident light is not focused on the mask, resulting in soft edges that blur the mask contours. Therefore, an approach to compensate for soft edges is necessary to present a sharp image with this approach [14].

Relay lenses are generally used to present a hard-edge mask to focus incident light onto an occlusion mask. This method has limitations in terms of form factor, viewing angle, and diffraction artifacts. Recently, several methods have been proposed, including a hard-edge occlusion mask that can be added to conventional OST-HMDs [54], viewing angle expansions for OCOST-HMDs using elliptical mirrors [53], and removal of diffraction artifacts using photochromic materials [4, 35]. There are also methods for implementing varifocal occlusion by physically [9] or optically [12, 39] controlling the distance of the mask from the eye. Our StainedSweepercan realize LAD with a single DMD as well as these OCOST-HMDs; thus, these optical designs of OCOST-HMDs with a single SLM can be applied to our system.

Unlike OCOST-HMDs, LAD [15, 19] does not simply use a black occlusion mask but instead uses polarizing optical elements that act as spatial color filters. Functionally, the LAD is expected to improve power consumption and dynamic range over conventional OCOST-HMDs that fill the field of view with black and add color on top. In addition, the LAD experiment will lead to the concept of multispectral OCOST-HMDs. In other words, since LAD manipulates light on a spectral basis, it can be expected to be applied to flexible visual appearance control compared to conventional RGB displays. However, controlling both brightness and color with current LADs requires 2 [15] or 3 [19] SLMs (Fig. 2), which hinders the practical form factor. In this paper, we present an LAD that can control both brightness and color with a single SLM.

2.2 Multi-spectral Displays

Our system can display light-attenuated images in the field of view consisting of light with different spectra passing through a color filter by time-multiplexing with a DMD. This idea can be seen as an application of the image formation method of a multispectral projector to an OST-HMD. Conventional Digital Lighting Processing (DLP) projectors present three primary color images by synchronizing the emission

timing of RGB light sources such as LEDs with the flip pattern of the DMD. In contrast, a multispectral projector has been proposed that presents images by replacing these RGB light sources with light sources of different spectra.

These multispectral displays can display high-fidelity images close to reality by taking metamerism into account [8]. Methods of combining light sources of different spectra include: using multiple light sources to increase the number of primary colors [20, 29]; spectralizing a white light source using a diffraction grating [34, 49] or prism [40] and then passing only light of specific wavelengths through a DMD; and passing a white light source through a time-synchronized narrowband tunable color filter and a DMD [10]. Our approach is close to the last one.

In multispectral projectors, polarizing color filters, such as the Lyot [30] and Solc [45] filters, are used as narrowband color filters. To achieve narrow bandwidth with these filters, the number of waveplates that make up the filter must be very large, making it impractical to fit them into the form factor of an HMD. In addition, the narrower the bandwidth of the filter, the lower the light transmittance, making it difficult to apply to LADs, while it can be applied to projectors that can project strong light. We propose an optimization algorithm that takes into account the trade-off between bandwidth and higher transmittance of the color filter to introduce these polarized color filters into LADs.

2.3 OST-HMDs with High-speed Time-multiplexing

Several near-eye displays have been investigated to create a novel visual experience through high-speed synchronous control of programmable light sources and optics. Ueda et al. proposed IlluminatedFocus, which spatially defocused real-world vision by time-multiplexing a high-speed projection and a focus-tunable lens [44]. Koutaki and Shirai proposed near-eye displays that provide simultaneous images from multiple viewpoints by synchronously controlling a DLP projector and active shutter glasses [23, 24]. Our system study applies these programmable light sources and synchronous optical sweeps to LAD.

3 SOLC FILTER

As a polarized color filter for StainedSweeper, we focus on the reflective folded Solc filter [33]. This reflective design can achieve the same effect with half the number of retarders of conventional designs, contributing to a smaller form factor and a wider color gamut of the system. In addition, this filter works well with LADs that use a reflective optical design.

In this section, before introducing the optical design and control algorithms of StainedSweeper, we formulate the reflective folded Solc filter used in StainedSweeper.

3.1 Jones Calculation for Retarders

A polarization-based color filter consists of a retarder placed between two linear polarizers to modulate the transmittance of incident light according to its wavelength. For polarization analysis, we introduce Jones calculus [28], which can model the behavior of polarization states with linear calculations. Using the Jones matrix, a retarder $\mathbf{M}(\phi)$ that delays the incident light by a phase ϕ can be defined as

$$\mathbf{M}(\phi) := \begin{bmatrix} e^{-i\phi} & 0 \\ 0 & e^{i\phi} \end{bmatrix}. \quad (1)$$

Common retarders, such as quartz or polymer waveplates, have a wavelength-dependent phase delay, i.e., $\phi = \phi(\lambda)$. To simplify the notation, this argument is omitted when it is not necessary. Similarly, we denote $\mathbf{M} = \mathbf{M}(\phi)$ unless otherwise specified.

Let $\mathbf{M}_\theta(\phi)$ be the retarder rotated axially at an angle θ. $\mathbf{M}_\theta(\phi)$ is given by

$$\mathbf{M}_\theta(\phi) = \mathbf{R}_\theta^\mathsf{T} \mathbf{M}(\phi) \mathbf{R}_\theta$$
$$\text{where} \quad \mathbf{R}_\theta = \begin{bmatrix} \cos\theta & \sin\theta \\ -\sin\theta & \cos\theta \end{bmatrix}. \quad (2)$$
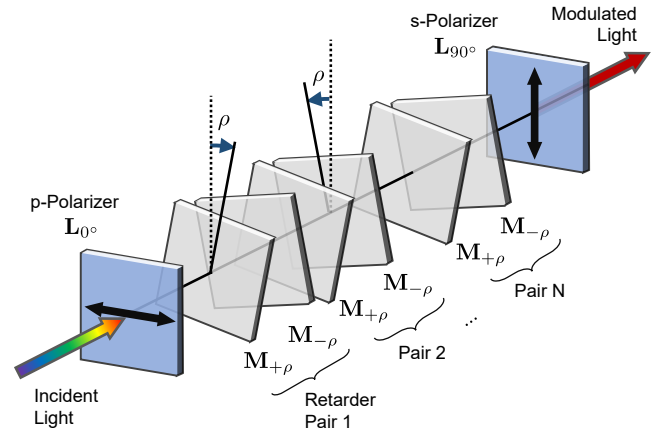

Fig. 4. Folded Solc Filter. The waveplates are rotated at the same angle ρ in alternate directions with respect to the optical axis. By sandwiching them between orthogonal polarizing plates, we obtain a polarized color filter.

3.2 Folded Solc Filter

The Solc filter consists of a stack of retarders at different angles with respect to the axial direction. By placing linear polarizers before and after this retarder group, the light intensity can be attenuated according to the wavelength of the incident light.

In particular, the folded Solc filter (Fig. 4) [45] arranges retarders with the same phase retardance $\mathbf{M}(\phi)$ to have alternating equal azimuthal tilts ρ. When N retarders (N: even) are arranged, the angle of rotation of each retarder θ_k ($k = 1, \cdots, N$) is given by $\theta_k = (-1)^{k-1}\rho$.

We denote the Solc filter with N retarders as $\mathbf{M}_{\text{Solc},N}$, which can be calculated as

$$\mathbf{M}_{\text{Solc},N} = \mathbf{L}_{90°} \underbrace{(\mathbf{M}_{-\rho}\mathbf{M}_{+\rho}) \cdot (\mathbf{M}_{-\rho}\mathbf{M}_{+\rho}) \cdots (\mathbf{M}_{-\rho}\mathbf{M}_{+\rho})}_{N/2} \mathbf{L}_{0°} \quad (3)$$

where $\mathbf{L}_{0°}$ and $\mathbf{L}_{90°}$ are the ideal linear polarizers with horizontal (p-polarized, $0°$) and vertical (s-polarized, $90°$) transmission axes that can be defined as

$$\mathbf{L}_{0°} := \begin{bmatrix} 1 & 0 \\ 0 & 0 \end{bmatrix}, \quad \mathbf{L}_{90°} := \begin{bmatrix} 0 & 0 \\ 0 & 1 \end{bmatrix}. \quad (4)$$

From Eq. (2), $\mathbf{M}_{+\rho}$ is calculated as (see Supp. Sec. A.1)

$$\mathbf{M}_{+\rho} = \begin{bmatrix} \cos\phi - i\cos 2\rho \sin\phi & -i\sin 2\rho \sin\phi \\ -i\sin 2\rho \sin\phi & \cos\phi + i\cos 2\rho \sin\phi \end{bmatrix}. \quad (5)$$

Now we denote each element of matrix $(\mathbf{M}_{-\rho}\mathbf{M}_{+\rho})^{N/2}$ as

$$(\mathbf{M}_{-\rho}\mathbf{M}_{+\rho})^{N/2} := \begin{bmatrix} m_{11,N} & m_{12,N} \\ m_{21,N} & m_{22,N} \end{bmatrix}. \quad (6)$$

By substituting Eq. (6) into Eq. (3), we obtain

$$\begin{aligned} \mathbf{M}_{\text{Solc},N} &= \mathbf{L}_{90°}(\mathbf{M}_{-\rho}\mathbf{M}_{+\rho})^{N/2}\mathbf{L}_{0°} \\ &= \begin{bmatrix} 0 & 0 \\ m_{21,N} & 0 \end{bmatrix}. \end{aligned} \quad (7)$$

From [51], making use of Chebyshev polynomials, the expression for $m_{21,N}$ is given by

$$m_{21,N} = -\sin N\rho \sin^2\phi \cdot \frac{\sin(N\Lambda/2)}{\sin\Lambda}$$
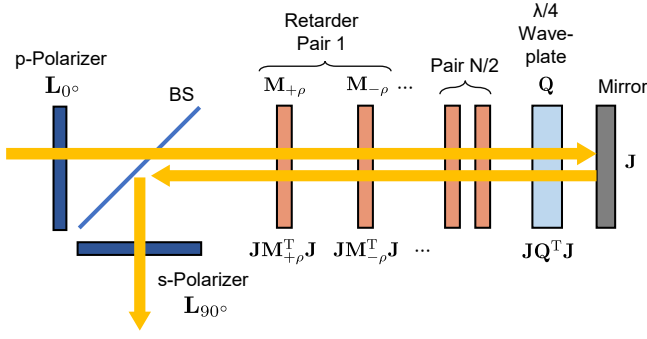$$\text{where} \quad \Lambda = \cos^{-1}(\cos^2\phi - \sin^2\phi \cos N\rho). \quad (8)$$

Fig. 5. Reflective Folding Solc Filter. The reflective design doubles the number of waveplates in the Solc filter.
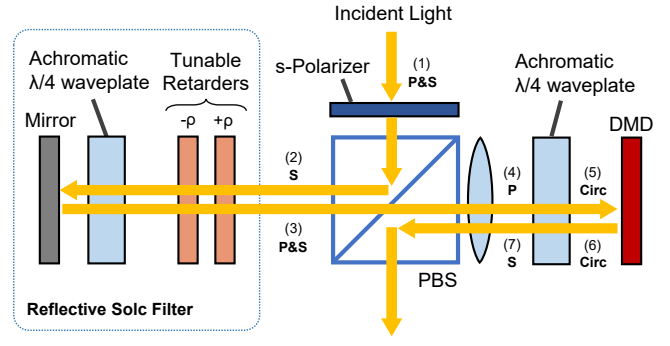

Fig. 6. Schematic of the see-through optical design of our StainedSweepersystem with $N = 4$ configuration. The yellow arrows indicate the light path of incident light from the real world.

As a result, the wavelength-dependent intensity of the Solc filter is given as $I_N(\lambda) = \|m_{21,N}\|^2$.

ρ is typically chosen as $\rho = \pi/4N$ to maximize transmitted energy. In particular, when $N = 4$ and $\rho = \pi/16 = 11.25°$, we obtain (see Supp. Sec. A.2)

$$
\begin{aligned}
m_{21,4} &= -2\sin 4\rho \sin^2 \phi (\cos^2 \phi - \sin^2 \phi \cos 4\rho) \\
&= -\sin^2 \phi (\sqrt{2}\cos^2 \phi - \sin^2 \phi).
\end{aligned}
\tag{9}
$$

3.3 Reflective Folded Solc Filter

Figure 5 shows the schematic of the reflective folded Solc filter [33]. The reflective folded Solc filter can achieve the same effect with half the number of retarders of its conventional design.

In the reflective folded Solc filter, when trying to create N pairs of filters, the filter consists of $N/2$ retarders alternately rotated by the angle ρ, a quarter-wave retarder and a mirror. The quarter-wave retarder should have wavelength-independent retardance, such as a Fresnel-Romb retarder or an achromatic retarder.

The Jones matrix of the mirror $\mathbf{J}$ and the wavelength-independent quarter-wave retarder $\mathbf{Q}$ is defined by

$$
\mathbf{J} := \begin{bmatrix} 1 & 0 \\ 0 & -1 \end{bmatrix}, \quad \mathbf{Q} := \begin{bmatrix} 1 & 0 \\ 0 & i \end{bmatrix}.
\tag{10}
$$

The retarder $\mathbf{M}$ working in the back passage after reflection from the mirror is described by the Jones matrix product $\mathbf{JM}^T\mathbf{J}$. Using this, a reflective folded Solc filter $\mathbf{M}_{\text{Refl},N}$ with $N/2$ retarders is given by

$$
\begin{aligned}
\mathbf{M}_{\text{Refl},N} = &\underbrace{(\mathbf{JM}^T_{+\rho}\mathbf{J})(\mathbf{JM}^T_{-\rho}\mathbf{J})\cdots(\mathbf{JM}^T_{+\rho}\mathbf{J})(\mathbf{JM}^T_{-\rho}\mathbf{J})}_{N/2} \\
&\cdot(\mathbf{JQ}^T\mathbf{J})\cdot\mathbf{J}\cdot\mathbf{Q}\cdot\underbrace{\mathbf{M}_{-\rho}\mathbf{M}_{+\rho}\cdots\mathbf{M}_{-\rho}\mathbf{M}_{+\rho}}_{N/2}.
\end{aligned}
\tag{11}
$$

From Eq. (5) and (10), we obtain

$$
\mathbf{J}^2 = \mathbf{I}, \quad \mathbf{JQ}^T\mathbf{J} = \mathbf{Q}, \quad \mathbf{QJQ} = \mathbf{I},
\tag{12}
$$

$$
\mathbf{M}^T_{\pm\rho} = \mathbf{M}_{\pm\rho}, \quad \mathbf{JM}_{\pm\rho}\mathbf{J} = \mathbf{M}_{\mp\rho}.
\tag{13}
$$

By substituting Eq. (12) and (13) into Eq. (11), we obtain

$$
\begin{aligned}
\mathbf{M}_{\text{Refl},N} &= \underbrace{\mathbf{M}_{-\rho}\mathbf{M}_{+\rho}\cdots\mathbf{M}_{-\rho}\mathbf{M}_{+\rho}}_{N} \\
&= (\mathbf{M}_{-\rho}\mathbf{M}_{+\rho})^{N/2}.
\end{aligned}
\tag{14}
$$

From Eq. (7) and (14), when this stack of optical elements is sandwiched between linear polarizers, it can be confirmed that this reflective Solc filter has the same polarization characteristics as the conventional ones:

$$
\mathbf{M}_{\text{Solc},N} = \mathbf{L}_{90°}\mathbf{M}_{\text{Refl},N}\mathbf{L}_{0°}.
\tag{15}
$$

4 STAINEDSWEEPER

This section describes the outline of StainedSweeper. First, we introduce the optical design of the LAD using a folded Solc filter and a DMD (Sec. 4.1). Then, since our system uses tunable waveplates, we extend the Solc filter formulation to the case where each waveplate has a different delay (Sec. 4.2). From the color filter calculated in this formulation, we introduce how the primary colors used for time multiplexing are selected (Sec. 4.3). Finally, we present an optimization to reproduce the target color by synchronously controlling the DMD and the color filter (Sec. 4.4).

4.1 Optical Design

Figure 6 shows the schematic of our StainedSweeper. As in [15], our system achieves a see-through configuration by folding the optical path back through a polarizing beam splitter (PBS) and introducing light into a reflective Solc filter and DMD in sequence. We use two tunable retarders in the reflective Solc filter, i.e., $N = 4$.

A PBS splits unpolarized incident light into p- and s-polarized light, with the p-polarized light passing through the PBS and the s-polarized light being reflected. By placing a PBS in front of the reflective Solc filter, we obtain $\mathbf{M}_{\text{Solc},4}$ as if the filter $\mathbf{M}_{\text{Refl},4}$ were sandwiched between $\mathbf{L}_{0°}$ and $\mathbf{L}_{90°}$ (Eq. (15)).

Light passing through the reflective Solc filter enters the DMD, which has a lens and an achromatic $\lambda/4$ plate in front of it. The lens is used to focus light from infinity onto the DMD, and the achromatic quarter $\lambda/4$ is used to convert the p-polarized light to the s-polarized light so that the light is reflected back to the PBS. This waveplate should be achromatic to minimize wavelength-dependent light attenuation.

Following the arrows in Fig. 6, we describe the optical path of incident light to the eye: (1) unpolarized incident light passes through a 0° linear polarizer and becomes s-polarized. (2) This s-polarized light is reflected by the PBS and enters the reflective Solc filter. (3) The Solc filter uniformly modulates the phase of the incident light so that the output light is a mixture of p- and s-polarized light. (4) Only p-polarized light passes directly through the PBS to the waveplate to change its polarization state to circular polarization. (5) The light enters the DMD, which modulates the amplitude of the incident light. Finally, (6) the reflected light from the DMD is again changed to (7) s-polarized, and the PBS reflects the light to reach the eye.

4.2 Solc Filter for Different Retarders

We use tunable LC retarders, which can change the retardation phase by input voltage. Although in Sec. 3 we assumed that the phase delay ϕ of the two retarders is the same, in this system the delays of the two retarders can be different. Therefore, we extend the Solc filter formulation to the case of waveplates with different delays.

We denote the voltages applied to the tunable waveplates 1 and 2 by V_1 and V_2, and the delays of each waveplate as $\phi_1(V_1, \lambda)$ and $\phi_2(V_2, \lambda)$, respectively. In general, ϕ_1 and ϕ_2 are different because the tunable

waveplates have different delay characteristics. Hence, Eq. (14) can be rewritten as

$$\mathbf{M}_{\text{Refl},4} = \mathbf{M}_{-\rho}(\phi_1)\mathbf{M}_{+\rho}(\phi_2)\mathbf{M}_{-\rho}(\phi_2)\mathbf{M}_{+\rho}(\phi_1). \quad (16)$$

Also, when $\rho = \pi/16$, Eq. (9) can be rewritten as (see Supp. Sec. B)

$$m_{21,4}(\phi_1,\phi_2) = -\sin\phi_1\sin\phi_2(\sqrt{2}\cos\phi_1\cos\phi_2 - \sin\phi_1\sin\phi_2)$$
$$-\frac{1}{\sqrt{2}}\sin(\phi_1-\phi_2)\sin(\phi_1+\phi_2). \quad (17)$$

4.3 Selecting Primary Colors

From the color filters calculated in Eq. (17), we select the primary colors to be used for time multiplexing. When multiple colors are mixed at high speed, the human eye perceives the color as its integral. In other words, the gamut that can be represented by time-multiplexing is the area that can be represented as a linear sum of the primary colors. For example, when red and blue are rapidly alternated, the human eye perceives purple, an intermediate color on the *xy* chromaticity diagram.

To maximize the colors that can be represented by the linear sum of the primary colors, first take as large a polygonal area as possible on the *xy* chromaticity diagram with the primary colors as vertices. In addition, the intensity of the primary colors should be as light as possible to lighten the intensity of the reproduced color obtained by the weighted sum of the primary colors.

Based on the above conditions, we select M primary colors from the 2D color filter distribution stretched by ϕ_1 and ϕ_2. We are currently using an exploratory method to select candidates for primary colors. First, we extract the points in the color filter where the intensity is 50 % or more and calculate their convex hull on the *xy* chromaticity diagram. Then, among the points that make up the convex hull, the points that maximize the area of the polygon stretched by the M points are selected as the primary colors. Specifically, the two points farthest from the points forming the convex hull are selected first as the start and end points. Then, selecting $M-2$ points at random from the remaining points is iterated 1.0×10^5 times, and the points with the largest area of the polygon with sides M are selected as primary colors.

Note that the primary colors obtained by this method are not necessarily the globally optimal solution. However, as shown in Sec. 6, the primary colors support a sufficient color gamut to demonstrate our concept.

4.4 Optimizing Time-multiplexing Matrix

Based on the selected primary colors, we optimize the time multiplexing schedule as a linear matrix. From this, we represent the color vectors using the CIEXYZ color system: $\mathbf{c} = [c_X, c_Y, c_Z]^{\text{T}}$. If we reproduce L target colors $\{\mathbf{c}_i\}_{i=1}^L$ using the primary colors $\{\mathbf{p}_j\}_{j=1}^M$ and the time-multiplexing ratio t_{ij}, the following linear summation holds:

$$\begin{bmatrix} t_{11} & \cdots & t_{1M} \\ \vdots & \ddots & \vdots \\ t_{L1} & \cdots & t_{LM} \end{bmatrix} \cdot \begin{bmatrix} \mathbf{p}_1^{\text{T}} \\ \vdots \\ \mathbf{p}_M^{\text{T}} \end{bmatrix} = \begin{bmatrix} \mathbf{c}_1^{\text{T}} \\ \vdots \\ \mathbf{c}_L^{\text{T}} \end{bmatrix}$$
$$\Leftrightarrow \quad \mathbf{T} \cdot \mathbf{P} = \mathbf{C} \quad (18)$$

where $\mathbf{T} = [t_{ij}] \in \mathbb{R}^{L \times M}$ is the mixture matrix for time-multiplexing, $\mathbf{P} = [\mathbf{p}_1^{\text{T}}, \cdots, \mathbf{p}_M^{\text{T}}]^{\text{T}} \in \mathbb{R}^{M \times 3}$ is the primary color matrix, and $\mathbf{C} = [\mathbf{c}_1^{\text{T}}, \cdots, \mathbf{c}_L^{\text{T}}]^{\text{T}} \in \mathbb{R}^{L \times 3}$ is the target color matrix.

We consider optimizing $\mathbf{T}$ from the given $\mathbf{P}$ and $\mathbf{C}$. Since $M < L$ in general, Eq. (18) is an over-determined problem. To optimize $\mathbf{T}$, we define the objective function as the non-linear programming problem:

$$\underset{\mathbf{T}}{\text{minimize}} \|\mathbf{T} \cdot \mathbf{P} - \alpha\mathbf{C}\|_F^2 \quad \text{s.t.} \quad \mathbf{T} \geq 0, \sum_{j=1}^M \max_i t_{ij} = 1 \quad (19)$$

where $0 < \alpha < 1$ is the ratio of the intensity of the reproduced color to the target color.
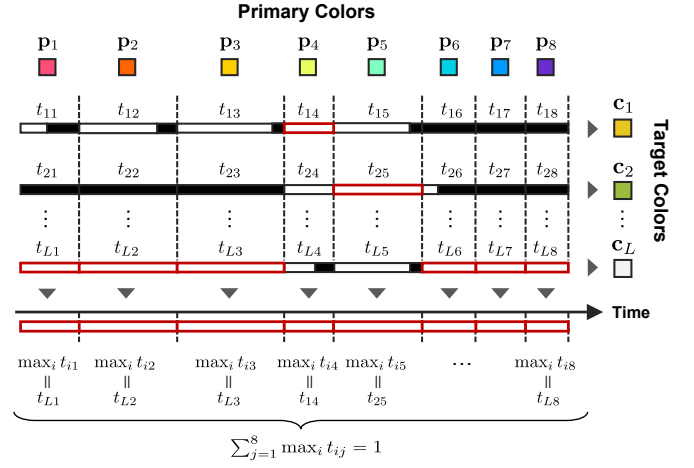

Fig. 7. Time-multiplexed matrix $\mathbf{T}$ in time sequence. In the bar showing each element t_{ij}, white and black indicate the time when the DMD is on and off, respectively. The red framed bar indicates the maximum duration $\max_i t_{ij}$ that the DMD is on when attempting to reproduce the target color $\mathbf{c}_i$ using each primary color $\mathbf{p}_j$. The constraint is set so that when these maximum durations are arranged in a time series, its sum is 1 (i.e., unit time).
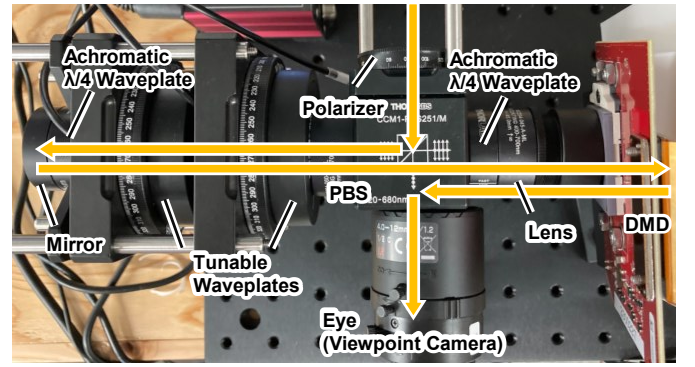

Fig. 8. Hardware setup of our experiment. The schematic is identical to Fig. 6.

Figure 7 outlines the constraints in Eq. (19). First, since $\mathbf{T}$ is a scheduling matrix of the time-multiplex control, $t_{ij} \geq 0$ is given as a constraint. Next, the maximum time $\max_i t_{ij}$ for each column of $\mathbf{T}$ determines the maximum time that each primary color can be displayed. Since the time multiplexing of all primary colors must be completed per unit of time, $\sum_{j=1}^M \max_i t_{ij} = 1$ is given as a constraint. On the other hand, due to this constraint, all elements of t_{ij} are less than 1. Therefore, Eq. (18) does not hold in almost all cases, and $\mathbf{T} \cdot \mathbf{P} < \mathbf{C}$. In other words, the reproduced color will always be darker than the target color. As a result, we introduce a hyperparameter α that controls how dark the reproduced color can be tolerated relative to the target color. A small value of α improves color reproducibility, but the reproduced colors become darker. Also, if α is large, the reproduced colors become lighter, but the color reproducibility deteriorates significantly.

5 IMPLEMENTATION

5.1 Hardware Setup

Figure 8 shows our hardware setups. We used Thorlabs LCC1421-A half-wavelength LC retarders as tunable waveplates. Because tunable waveplates have individual differences in retardation characteristics, each waveplate is accompanied by a retardation curve according to the input voltage at $\lambda_{635} = 635$ nm measured by the manufacturer. Figure 9 shows the curves $\phi_1(\lambda_{635}, V)$ and $\phi_2(\lambda_{635}, V)$ for the two tunable waveplates used in our prototype.
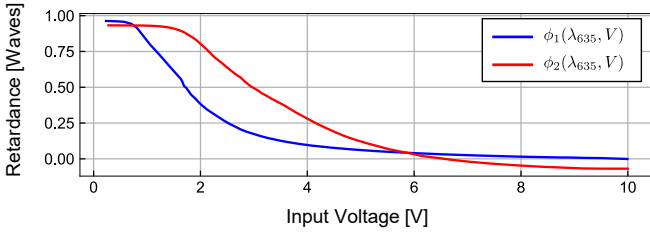
Fig. 9. The retardation curves $\phi_1(\lambda_{635}, V)$ and $\phi_2(\lambda_{635}, V)$ when a voltage V is applied to the tunable waveplates.

Fig. 10. The wavelength-dependent transmittance $\eta(\lambda)$ of the entire optical system.

For our simulation, it is necessary to interpolate the retardance at different wavelengths because the manufacturer's data sheet only provides retardance at 635 nm. Theoretically, the retardance in a wavelength plate can be derived from $\phi(\lambda) = 2\pi d \Delta n / \lambda$, where d is the thickness of the waveplate and Δn is the birefringence index of the LC material used. From this we interpolated the retardance at all wavelengths by $\phi(\lambda, V) = (\lambda/635) \cdot \phi(\lambda_{635}, V)$.

The tunable waveplates are mounted on a Thorlabs LCRM2/M rotary mount to properly set the rotation angle $\rho = 11.25°$. Each tunable waveplate is connected to the Thorlabs KLC101 LC controller and supplied with the appropriate voltage. When the analog input of the LC controller is turned on, the output voltage of the controller is set by an external input signal at the MOD IN connector. An external input of 0 to 5.0 V DC corresponds to an output voltage of 0 to ±25 Vrms.

For a DMD and its controller, we used a Digital Light Processing (DLP) projector evaluation module (DLP LightCrafter 6500 from Texas Instruments, with a resolution of 1920 × 1080 pixels). We also used a microcontroller (NUCLEO-F303K8 from STMicroelectronics, operating at 72 MHz) to output analog voltage values to control the LC controllers. A digital-to-analog converter (DAC) built into the microcontroller generated the analog voltage. However, since the output of this DAC has a too high impedance to be used to control the LC controller, it was connected to the LC controllers via a voltage follower circuit using an operational amplifier (NJU7043D from Nisshinbo Micro Devices). The method of synchronizing the DMD and LC controllers using this microcontroller is described in Sec. 5.2.

Other components were from Thorlabs: LPVISE100-A for linear polarizers, AQWP10M-580 for achromatic $\lambda/4$ wave plates, PBS251 for a PBS, BB1-E02 for a mirror, and AC254-045-A for a lens. In the prototype, the form factor was L 56mm × W 165 mm × H 56 mm. Note that in the current setup, the total length of the reflective Solc filter is about 60 mm, which causes a large form factor and a narrow field of view. An improvement to this problem is discussed in Sec. 9.2.

We used a color camera (a2A2590-60ucBAS from Basler, resolution 2592 × 1944 pixels) with a varifocal lens (M12VM412 from TAMRON) as a user-perspective camera.

5.2 Synchronous Control of DMD and Solc Filter

In order for the proposed system to function as a display, it is necessary to synchronously control the various primary colors and their corresponding spatial patterns and display these patterns by high-speed time multiplexing. Since we use a DMD as the spatial pattern control element, the DMD and the Solc filter are controlled synchronously. In such systems, synchronization is usually achieved by inputting a trigger signal, but the implementation tends to be complicated, and the data format describing the control of the DMD and the Solc filter is also proprietary and dependent on the implementation.

Therefore, based on the idea of the previous system [18], we focused on the ability of the DMD controller to control LED colors in synchronization with the DMD. Because DMDs are typically used as DLPs, the DMD controller has a built-in timing control function to synchronize the DMD controller with the LED light source. For each LED color control signal, the microcontroller interprets the signal and generates a corresponding control signal for the LC controller of the Solc filter based on predefined mappings. This ensures that the displayed primary color matches the intended LED color. Since the DMD controller can
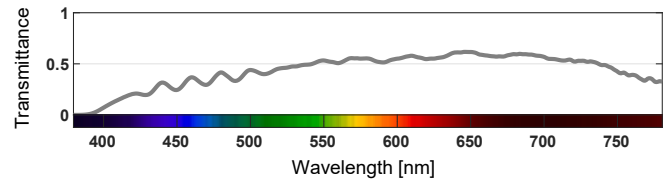
output ON/OFF control signals for each of the three channels (red, green, and blue), a total of $2^3 = 8$ patterns can be expressed. In response to the signal input of these eight patterns, the microcontroller outputs, via a DAC, the set voltage values of the two LC controllers to display the corresponding primary colors. In this way, we can control the display of the eight primary colors in synchronization with the DMD patterns.

Using this control method, we can set up a synchronous control sequence for the DMD and the Solc filter using the development software (DLP LightCrafter DLPC900 GUI from Texas Instruments) without modification. The default format of the development software can be used to save and load configuration data. This allows researchers or engineers experienced in designing DLP projectors with DMD control to immediately become familiar with the proposed system and begin controlling it.

5.3 Transmittance of Each Optical Element

In general, optical elements attenuate light in a wavelength-dependent manner. Therefore, when simulation and actual measurement are compared, it is necessary to correct this by multiplying the Solc filter by the wavelength-dependent transmittance of all optical elements in the simulation.

Figure 10 shows the wavelength-dependent transmittance $\eta(\lambda)$ of the entire optical system, calculated from the transmittance of the optical system based on the manufacturer's specifications. From Fig. 6, the optical path through the system transmits once through the polarizer, reflects twice, and transmits once through the PBS, transmits four times through the tunable waveplate, and transmits four times through the $\lambda/4$ waveplate. Of these, the tunable waveplate and polarizer have low transmittance in the short wavelength band. As a result, the light coming out of the optical system is closer to red than ideal. The final filter characteristics $I_{out,4}(\lambda) = \eta(\lambda) \|m_{21,4}\|^2$.

6 SIMULATION

Prior to the actual measurements, we simulated the expected color filter characteristics of the prototype by discretely sampling voltages from 0 V to 8 V in 0.02 V increments and calculating $I_{out,4}(\lambda)$. We then performed optimization with $\alpha = 0.4$ setting the colors in the color chart (Fig. 1b) ($L = 25$) as the target colors, then comparing the reproduced colors with the target colors. We use MATLAB R2022a for this optimization.

6.1 Characteristics of Color Filters

First, we describe the characteristics of the color filters obtained by simulation. The top row of Figure 12 shows the simulated color filter characteristics for the two tubular retarders used in the prototype. In the following, we refer to this top row when we refer to Fig. 12.

Fig. 12 (a) shows the distribution of filters on the xy chromaticity diagram. In the simulation, the convex hull of the filters by this system covers 68.6 % of sRGB. After selecting the primary colors of this convex hull, the area of the primary colors was 67.7 % of sRGB.

Fig. 12 (b) visualizes the color and intensity of the filters with respect to V_1 and V_2. For the tunable waveplates used in our prototype, the filters with high chroma and high intensity occupy the regions of 1.1 V $< V_1 <$ 2.5 V and 2.2 V $< V_2 <$ 4.3 V, approximately corresponding to the range $0.25\lambda < \phi_{1,2} < 0.75\lambda$ of Fig. 9.
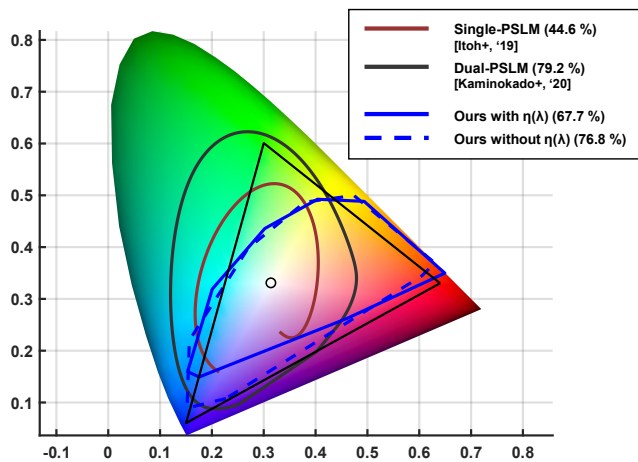
Fig. 11. Comparison of the gamut of PSLM-based LAD [15, 19] and our method in simulation. Phase delays φ in PSLM-based LADs are calculated by Eqs. (14) and (15) in [19]. The percentages in the legend indicate the percentage overlap with sRGB.

Fig. 12 (c) shows a comparison of the reproduced colors obtained by optimization and the target colors. The left-bottom of Fig. 12 (c) shows that the reproduced colors are exact approximations of the target colors in the polygon formed by the primary colors. Even for target colors outside the polygon, which in principle cannot be reproduced, it can be confirmed that the reproduced colors converge at neighboring points on the edges of the polygon. The right bottom of Fig. 12 (c) shows the visualization of the time-multiplexed matrix **T**. From the figure, we can see that our optimization can control color, where the contribution of the red primary color is high for a reddish target color, and intensity, where the overall contribution rate decreases as the brightness decreases from white to black.

6.2 Color Filter Comparison

Next, we compare the gamut reproduced by this system with the gamut reproduced by PSLM-based LADs. To simulate PSLM-based LADs, the retardation of each PSLM was calculated from the parameter estimation equations in the Dual-PSLM LAD paper (Eqs. (14) and (15) in [19]). In addition, we compare the gamut with the case of an ideal optical system with uniform transmittance in visible light, i.e. the color filters calculated without $\eta(\lambda)$, because our system tends to cut off the short-wavelength band throughout the optical system.

Figure 11 shows the comparison of the color filters. From Fig. 11, the color filter in our 1-SLM setup has sRGB sufficiency equivalent to that of a dual-PSLM setup (3 SLMs if intensity modulation is also included) in an ideal optical system. Considering the transmittance of the optical system, it can be seen that the color gamut is reduced in the short wavelength band, i.e., near the blue region. However, even in this case, our 1 SLM system is capable of supporting a color gamut nearly ×1.5 larger than that of a single PSLM setup (2 SLMs if intensity modulation is included). Also, although this is due to the characteristics of the LC used, the PSLM-based LAD can express the green side of the gamut well, but the red side of the gamut is less expressive. On the other hand, our system shows high expressiveness on the red side of the gamut.

7 VERIFICATION

This section presents the results of the actual measurement of the color filter by the prototype. First, we explain the setup of the filter measurement, then we present the measurement results and the comparison with the simulation.

7.1 Measurement Setup

For the color filter measurements, we first placed a white reference light source in front of the system and measured the spectrum of light passing through the system with a spectrometer while changing the voltages of the tunable waveplates. The color filter characteristics were then calculated by dividing the spectrum measured by the spectrometer by the spectral distribution of the light source.

We used a Thorlabs SOLIS-3C High-Power LED 5700K (Day Light White) with a DC2200 High-Power 1-Channel LED Driver as a reference light source. Fig. 13 shows the light source spectrum measured by a spectroradiometer (UPRTek MK350N Premium), which has a measurement range of 380 to 780 nm with a measurement step of 1 nm. We discretely sample voltages from 0 V to 8 V in 0.08 V increments for both tunable waveplates.

As in Sec. 6, the primary colors were selected from these color filters and the multiplexed matrix was optimized to reproduce the target colors.

7.2 Results

The bottom row of Figure 12 shows the actual measured color filter characteristics. In the following, we refer to this bottom row when we refer to Fig. 12.

Figure 12 (b) shows that the distribution of the color filter characteristics with respect to the input voltage is roughly the same between the simulation and the measurement, confirming that there is little discrepancy in the simulation. On the other hand, in the *xy* chromaticity diagram (Fig. 12 (a)), the color gamut is reduced in the actual measurement compared to the simulation, especially in the long-wavelength band (red color). Comparing the gamut sufficiency to sRGB, the simulation was 67.7 % while the actual measurement was 56.2 %. Actual measured values in the literature [19] state that the 2-SLM LAD and the 3-SLM LAD can support 41.4 % and 75.8 % of sRGB, respectively. Based on these results, our system can be considered as a gamut between conventional 2-SLM and 3-SLM LAD with only 1-SLM.

One of the main reasons for the degeneracy of the color gamut, especially in red, in the actual measurement compared to the simulation may be the chromatic dispersion property of the birefringence in the LC. The details of this discrepancy are discussed in Sec. 9.1.

Figure 12 (c) shows the result of optimization based on the measured data for the target color on the color chart image. The *xy* chromaticity diagram shows that the target colors are reproduced well even in the measured case. We also confirmed that the time-multiplexing matrix shows the same trend as in the simulation.

8 DEMONSTRATION

Using the measured color filters, we demonstrate the performance of our StainedSweeper by displaying the color chart image.

Figure 1 (c) shows the color chart image displayed on the system and captured by the viewpoint camera. When the images were captured, a standard white surface light source was placed in front of the viewpoint. Note that there is a color difference from the restored image (Fig. 1b, bottom) because it is difficult to perfectly adjust the white balance of the viewpoint camera. From the figure, it can be confirmed that the system can filter the incident light with a hue and brightness close to that of the input image, although the green direction is slightly faded. In Fig. 1 (d), a real object is placed in front of the system to confirm that our system is a see-through display. Even in this case, it can be confirmed that this system performs wavelength-dependent filtering of the incident light on a pixel-by-pixel basis, just like stained glass.

9 DISCUSSION AND FUTURE WORK

In this section, we discuss the remaining challenges to make our StainedSweeper system more practical and possible research directions.

9.1 Error between Simulation and Measurement

Although similarities were observed between simulations and measurements in terms of intensity and hue distribution (Fig. 12 b), differences were observed, especially in the highly saturated purple and red regions (Fig. 12 a).

One of the main reasons for this difference is the chromatic dispersion of the refractive index. In the simulations, it was assumed that the
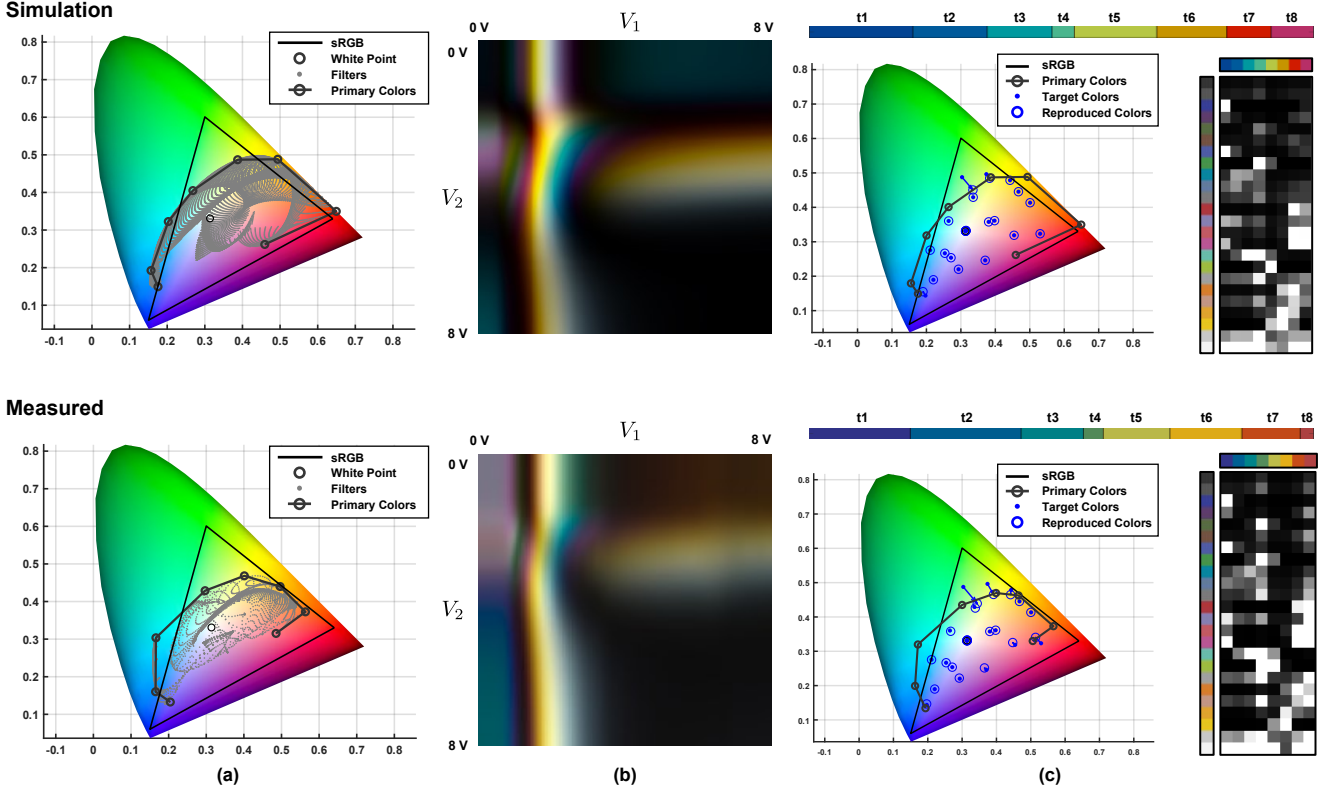
Fig. 12. Comparison of (top) simulated and (bottom) measured polarized color filter characteristics and optimization results using the color chart as target colors. (a) Color filter distribution (gray) and selected primary colors ($M = 8$, black line) for discrete voltage values applied to the two variable waveplates in the xy chromaticity diagram. Sampling was done in 0.02 V increments in the simulation and in 0.08 V increments in the actual measurement. (b) Visualization of the color filters for the voltage values applied to the two variable waveplates. (c, top) Each primary color $\mathbf{p}_j$ and maximum duration $\max_i t_{ij}$ obtained by optimization (see Fig. 7) (c, left-bottom) Comparison of the target colors (blue dots) and the reproduced colors obtained by optimization (blue circles) in the xy chromaticity diagram. (c, right bottom) Time-multiplexing matrix $\{t_{ij}\}$ of DMD to each primary color $\mathbf{p}_j$ to reproduce the target color $\mathbf{c}_i$. In this figure, the duration of each primary color is assumed to be equal.
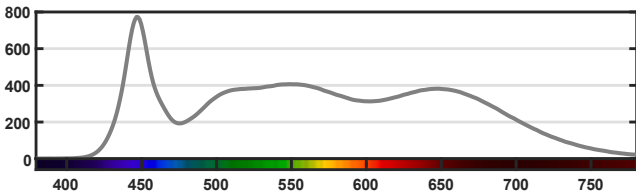

Fig. 13. The spectrum of the reference light for color filter measurements. The x-axis is the wavelength, and the y-axis is the irradiance [mW/m^2].

retardation varies linearly with wavelength. However, especially in LC materials, molecular polarization rates and electronic transitions produce a wavelength-dependent refractive index (chromatic dispersion). Therefore, birefringence is a wavelength-dependent function $\Delta n(\lambda)$. $\Delta n(\lambda)$ has a higher retardation at $\lambda < \lambda_{635}$, the reference wavelength, and a lower retardation at $\lambda > \lambda_{635}$.

In Sec. 6, the range of higher saturation and brightness of the color filter was $0.25\lambda < \phi < 0.75\lambda$. In reality, when the dispersion of the color is taken into account, the range in which ϕ falls within this range is narrower than in the simulation for both short and long wavelengths. Therefore, we reasoned that there would be a difference between the simulation and actual measurements in the range of highly saturated purples and reds. To accurately simulate this difference, $\phi(\lambda)$ should be accurately measured in various λ, and $\Delta n(\lambda)$ of LC materials should be approximated using an appropriate model, such as the Sellmeier formula [41].

9.2 Hardware Miniaturization

Although our system has a smaller configuration than previous systems with only 1 SLM, the current prototype is somewhat large for a wearable form factor. The limitations in form factor and viewing angle of the current prototype are largely due to the rotation fixture used to set $\rho = 11.25°$. The tunable retarder has dimensions of L 12 mm × W 6 mm × H 17mm without the mount (Thorlabs LCC1111U-A). Therefore, if the angle can be accurately fixed, the optics can be mounted at about L 38 mm × W 85 mm × H 38 mm, which is expected to realize a more wearable system. In addition, the total length of the reflective Solc filter will also be about 22 mm with this implementation, which is expected to expand its field of view.

BS is the other factor that limits the form factor of the system; in OCOST-HMD, BS is used even in the latest compact configurations because it should relay the incident light once to the SLM for occlusion [48]. Unlike conventional LADs, since our system consists of a single SLM, the optical system proposed in the area of OCOST-HMD can be applied directly to LADs. Therefore, if a more compact relay optical system is proposed for OCOST-HMD, its application to this system can be considered.

9.3 Extending Color Gamut

Although our system can display the same or better color gamut as existing LADs with a single SLM, it is not expressive enough compared to the sRGB color gamut. We present several directions for expanding the color gamut with our system.

Increasing the Number of Retarders A simple way to improve the gamut is to increase the number N of tunable wave plates that

8

make up the Solc filter. Although some multispectral projectors use narrowband polarizing color filters to expand the color gamut [10], the color filters are almost equivalent to increasing N to 20 $\sim$100 in our system, resulting in larger devices, higher cost and higher power consumption. As N increases, it is necessary to consider the optimal design based on the trade-off between the form factor and the required color gamut.

Sidelobe Reduction by Combining Different Filters   If the spectrum of the Solc filter is multimodal, the side lobes can be reduced and the color purity increased by combining another polarized filter with different bandpass characteristics. For example, the combination of a Solc filter with a Lyot filter of different bandwidths has been proposed to reduce sidelobes [50].

Using Achromatic Tunable Retarders   As shown in Fig. 11, the short-wavelength cut-off characteristics of tunable retarders significantly impact color reproducibility, especially in blue. If achromatic tunable retarders with less wavelength dependence can be introduced, it may be possible to improve the color gamut. Approaches that use the phase difference between two LC materials [1] and photonic metamaterials [2] have been investigated as such achromatic tunable retarders.

9.4   Reproduction of Arbitrary Target Colors

In this paper, $L = 25$ colors in the color chart image shown in Fig. 1 (b) were set as target colors, while arbitrary colors were not currently reproduced. Theoretically, once the time-multiplexed vector $\mathbf{t}_i = [t_{i1}, \cdots, t_{iM}]$ in Eq. (18) for the target color $\mathbf{c}_i$ is determined, it is possible to reproduce any color by linear summation of the time-multiplexed vectors. For example, it is possible to reproduce arbitrary colors by performing Delaunay division based on target colors on the xy chromaticity diagram (Fig. 12 c) and weighting arbitrary colors based on the vertices of the Delaunay triangle.

9.5   Adapting to Variable Lighting Conditions

Our prototype assumes that the spectrum of incident light is constant. In practice, however, indoor and outdoor lighting conditions change from moment to moment. In this case, the light reaching the eye is the multiplication of the color filter and the incident light at each pixel of the DMD. To deal with this condition, a method for estimating the spatio-temporal spectrum of light reaching the eye and an algorithm that can reproduce the target color for any incident spectrum in real time are required. Since the latter was discussed in Sec. 9.4, the former will be discussed here.

When presenting images on OST-HMDs to compensate for the light entering the eye, a common method is to use a camera coaxially aligned to the viewpoint [11, 27]. However, unlike the traditional method of capturing color images with a camera, our system is required to estimate the spectrum of light entering the eye. The simplest but most expensive approach is to place a multispectral camera coaxially. If the multispectrum is recovered accurately from the color image, a color camera could be placed [52]. Another possible approach is to place a monochrome camera that can capture the spectrum passing through the Solc filter and restore multispectral images of filtered incident light [46] since the Solc filter has bandpass characteristics for each wavelength band.

9.6   Considering Rise Time in Tunable Waveplates

Tunable LC waveplates have a time of rise and fall in the transition from the time a voltage is applied to the time the retardation reaches the target. For the tunable waveplate used in this prototype, the fall time is 0.26 ms when the voltage is increased from 1.18 V to 10 V at 22 °C and the rise time is 15.8 ms when the voltage is decreased from 10 V to 1.18 V.

Although the rise time specification is particularly large relative to the system's target frame rate of 25 fps (= 40 ms), Fig. 1 (c) shows that this slow rise does not significantly affect the resulting image. Theoretically, if $t = 0$ when the voltage is applied, the retardation $\phi(t)$ of the LC tunable waveplate is denoted as $\phi(t) \propto \tanh(\gamma t)$, where γ is the constant [26]. Therefore, a possible reason why the system can

present an image close to the target is that the retardation is much closer to the target at the beginning of the rise because of the characteristics of the tanh function. However, a deeper analysis of this phenomenon and system improvements are required to improve color reproduction by time integration.

Hardware improvements to overcome this problem include the use of a tunable waveplate with a shorter rise time [42] or the increase in the device temperature. On the software side, the simplest improvement is to arrange the applied voltages $V_{1,m}$ and $V_{2,m}$ of each filter m in ascending order, since the fall time is much faster than the rise time. A more advanced method requires an optimization algorithm that takes into account rising and falling transitions as reformulate Eq. (18) as an integral for $\phi(t)$. Another possible method is to take reproduced images with the coaxial viewpoint camera (Sec. 9.5) and gradually improve the schedule matrix $\mathbf{T}$ using closed-loop control [38].

9.7   Mitigating Vergence-accommodation Conflict

Since the depth of field in our current prototype is fixed at infinity, Vergence-Accommodation Conflict (VAC) [13], the inconsistency between eye convergence and focal depth in HMDs, has not yet been resolved. However, unlike previous LADs that consisted of multiple SLMs, our system uses only a single SLM, making it easier to apply the various methods proposed in OCOST-HMD to solve VAC to LADs. For example, the recently proposed varifocal OCOST-HMDs solve VAC by physically [9] or optically [12, 39] shifting the distance of a single SLM. Our system can be easily extended to a varifocal setup by replacing the lenses in the optical system with the optics proposed in these methods.

9.8   Multispectral Additive VR/AR HMDs

Our system demonstrates how a multispectral color filter can be implemented on a near-eye display. In this work, we have implemented a subtractive multispectral near-eye display by filtering out real light. On the other hand, similar to a multispectral projector, an additive multispectral near-eye display can also be realized by filtering a white-light source instead of real light.

To the best of our knowledge, multispectral additive HMDs have not yet been realized. If our system can be implemented as a wearable form factor, as shown in Sec. 9.2, VR- and AR-HMDs that can add and subtract light in multispectral form could be realized, which would bring a rich visual expression close to reality to HMDs.

10   CONCLUSION

We presented StainedSweeper, a novel approach to LAD that can control both intensity and color on a single SLM by synchronously sweeping a DMD and a polarized color filter. To realize StainedSweeper, we designed a see-through optical system based on a reflective Solc filter, proposed a method to optimize the time-multiplexing matrix for the target color, and confirmed the effectiveness of this method with a prototype. Our system can display ×1.36 wider color range than conventional LAD with brightness and color control using 2 SLMs with DMD and PSLM (56.4 % fulfillment of sRGB color space versus 41.4%). Our system consists of only a single SLM, which provides flexibility in the future optical design of the LAD. We hope that this study will encourage researchers to explore further LAD design possibilities and improve virtual visual appearances through multispectral near-eye displays.

REFERENCES

[1] M. J. Abuleil and I. Abdulhalim. Tunable achromatic liquid crystal waveplates. *Optics Letters*, 39(19):5487–5490, Oct 2014.

[2] M. A. Aisheh, M. Abutoama, M. J. Abuleil, and I. Abdulhalim. Fast tunable metamaterial liquid crystal achromatic waveplate. *Nanophotonics*, 12(6):1115–1127, 2023.

[3] O. Cakmakci, Y. Ha, and J. P. Rolland. A compact optical see-through head-worn display with occlusion support. In *Proceedings of 3rd IEEE International Symposium on Mixed and Augmented Reality (ISMAR'04)*, pages 16–25, 2004.

[4] M. Chae, K. Bang, Y. Jo, C. Yoo, and B. Lee. Occlusion-capable see-through display without the screen-door effect using a photochromic mask. *Optics Letters*, 46(18):4554–4557, 2021.

[5] A. Erickson, K. Kim, G. Bruder, and G. F. Welch. Exploring the limitations of environment lighting on optical see-through head-mounted displays. In *Proceedings of the 2020 ACM Symposium on Spatial User Interaction (SUI'20)*, number 9, pages 1–8, New York, NY, USA, Oct. 2020.

[6] C. Gao, Y. Lin, and H. Hua. Occlusion capable optical see-through head-mounted display using freeform optics. In *Proceedings of 11th IEEE International Symposium on Mixed and Augmented Reality (ISMAR'12)*, pages 281–282, 2012.

[7] C. Gao, Y. Lin, and H. Hua. Optical see-through head-mounted display with occlusion capability. In *Proceedings of SPIE*, volume 8735, pages 87350F–1:9, 2013.

[8] A. Grundhöfer and D. Iwai. Recent advances in projection mapping algorithms, hardware and applications. *Computer Graphics Forum*, 37(2):653–675, 2018.

[9] T. Hamasaki and Y. Itoh. Varifocal occlusion for optical see-through head-mounted displays using a slide occlusion mask. *IEEE Transaction on Visualization and Computer Graphics*, 25(5):1961–1969, 2019.

[10] K. Hirai, D. Irie, and T. Horiuchi. Multi-primary image projector using programmable spectral light source. *Journal of the Society for Information Display*, 24(3):144–153, 2016.

[11] Y. Hiroi, Y. Itoh, T. Hamasaki, and M. Sugimoto. Adaptivisor: Assisting eye adaptation via occlusive optical see-through head-mounted displays. In *8th Augmented Human International Conference*, pages 9:1–9:9, New York, NY, USA, 2017. ACM.

[12] Y. Hiroi, T. Kaminokado, S. Ono, and Y. Itoh. Focal surface occlusion. *Optics Express*, 29(22):36581–36597, Oct 2021.

[13] D. M. Hoffman, A. R. Girshick, K. Akeley, and M. S. Banks. Vergence–accommodation conflicts hinder visual performance and cause visual fatigue. *Journal of vision*, 8(3):33–33, 2008.

[14] Y. Itoh, T. Hamasaki, and M. Sugimoto. Occlusion leak compensation for optical see-through displays using a single-layer transmissive spatial light modulator. *IEEE Transaction on Visualization and Computer Graphics*, 23(11):2463–2473, 2017.

[15] Y. Itoh, T. Langlotz, D. Iwai, K. Kiyokawa, and T. Amano. Light attenuation display: Subtractive see-through near-eye display via spatial color filtering. *IEEE Transaction on Visualization and Computer Graphics*, 25(5):1951–1960, May 2019.

[16] Y. Itoh, T. Langlotz, J. Sutton, and A. Plopski. Towards indistinguishable augmented reality: A survey on optical see-through head-mounted displays. *ACM Computing Surveys (CSUR)*, 2021.

[17] Y. Jiang, K. Zhou, and S. He. Human visual cortex responds to invisible chromatic flicker. *Nature Neuroscience*, 10(5):657–662, May 2007.

[18] I. Kamei, T. Hiraki, S. Fukushima, and T. Naemura. PILC projector: Image projection with pixel-level infrared light communication. *IEEE Access*, 7:160768–160778, 2019.

[19] T. Kaminokado, Y. Hiroi, and Y. Itoh. StainedView: Variable-Intensity Light-Attenuation display with cascaded spatial color filtering for improved color fidelity. *IEEE Transaction on Visualization and Computer Graphics*, 26(12):3576–3586, Dec. 2020.

[20] I. Kauvar, S. J. Yang, L. Shi, I. McDowall, and G. Wetzstein. Adaptive color display via perceptually-driven factored spectral projection. *ACM Trans. Graph.*, 34(6), nov 2015.

[21] K. Kim., D. Heo., and J. Hahn. Occlusion-capable head-mounted display. In *Proceedings of the 7th International Conference on Photonics, Optics and Laser Technology - Volume 1: PHOTOPTICS,*, pages 299–302. INSTICC, SciTePress, 2019.

[22] K. Kiyokawa, M. Billinghurst, B. Campbell, and E. Woods. An occlusion-capable optical see-through head mount display for supporting co-located collaboration. In *Proceedings of 2nd IEEE International Symposium on Mixed and Augmented Reality*, page 133, 2003.

[23] G. Koutaki. Binary continuous image decomposition for multi-view display. *ACM Transaction on Graphics*, 35(4):1–12, July 2016.

[24] G. Koutaki and K. Shirai. Multiplexing display using vector error propagation and smooth active shutter. In *ACM SIGGRAPH 2020 Emerging Technologies*, number Article 22 in SIGGRAPH '20, pages 1–2, New York, NY, USA, Aug. 2020. Association for Computing Machinery.

[25] B. Krajancich, N. Padmanaban, and G. Wetzstein. Factored occlusion: Single spatial light modulator occlusion-capable optical see-through augmented reality display. *IEEE Transaction on Visualization and Computer Graphics*, 26(5):1871–1879, 2020.

[26] G. Labrunie and J. Robert. Transient behavior of the electrically controlled birefringence in a nematic liquid crystal. *Journal of Applied Physics*, 44(11):4869–4874, 10 1973.

[27] T. Langlotz, M. Cook, and H. Regenbrecht. Real-time radiometric compensation for optical see-through head-mounted displays. *IEEE Transaction on Visualization and Computer Graphics*, 22(11):2385–2394, Nov. 2016.

[28] G. Lazarev, A. Hermerschmidt, S. Krüger, and S. Osten. Lcos spatial light modulators: trends and applications. *Optical Imaging and Metrology: Advanced Technologies*, pages 1–29, 2012.

[29] Y. Li, A. Majumder, D. Lu, and M. Gopi. Content-independent multi-spectral display using superimposed projections. *Computer Graphics Forum*, 34(2):337–348, 2015.

[30] B. Lyot. Optical apparatus with wide field using interference of polarized light. *Comptes Rendus de l'Académie des Sciences (Paris)*, 197(1593), 1933.

[31] A. Maimone and H. Fuchs. Computational augmented reality eyeglasses. In *Proceedings of 12th IEEE International Symposium on Mixed and Augmented Reality*, pages 29–38, 2013.

[32] A. Maimone, D. Lanman, K. Rathinavel, K. Keller, D. Luebke, and H. Fuchs. Pinlight displays: wide field of view augmented reality eyeglasses using defocused point light sources. In *ACM SIGGRAPH 2014 Emerging Technologies*, page 20, 2014.

[33] A. Messaadi, A. Vargas, M. M. Sánchez-López, P. García-Martínez, P. Kula, N. Bennis, and I. Moreno. Solc filters in a reflective geometry. *Journal of Optics*, 19(4):045703, Mar. 2017.

[34] A. Mohan, R. Raskar, and J. Tumblin. Agile spectrum imaging: Programmable wavelength modulation for cameras and projectors. *Computer Graphics Forum*, 27(2):709–717, 2008.

[35] C. W. Ooi, Y. Hiroi, and Y. Itoh. A compact photochromic occlusion capable see-through display with holographic lenses. In *2023 IEEE Conference Virtual Reality and 3D User Interfaces (VR)*, volume 0, pages 237–242, Mar. 2023.

[36] O. M. P. Santos, T. Gierlinger and S.André. The daylight blocking optical stereo see-through hmd. In *Workshop on Immersive projection technologies/Emerging display technologies*, page 4. ACM, 2008.

[37] T. C. Peck, J. J. Good, A. Erickson, I. Bynum, and G. Bruder. Effects of transparency on perceived humanness: Implications for rendering skin tones using optical See-Through displays. *IEEE Transaction on Visualization and Computer Graphics*, 28(5):2179–2189, May 2022.

[38] Y. Peng, S. Choi, N. Padmanaban, and G. Wetzstein. Neural holography with camera-in-the-loop training. *ACM Transaction on Graphics*, 39(6):1–14, Dec 2020.

[39] K. Rathinavel, G. Wetzstein, and H. Fuchs. Varifocal occlusion-capable optical see-through augmented reality display based on focus-tunable optics. *IEEE Transactions on Visualization and Computer Graphics*, 25(11):3125–3134, 2019.

[40] J. P. Rice, S. W. Brown, J. E. Neira, and R. R. Bousquet. A hyperspectral image projector for hyperspectral imagers. In *SPIE Proceedings*, volume 6565, pages 116–127. SPIE, April 2007.

[41] Sellmeier. Zur erklärung der abnormen farbenfolge im spectrum einiger substanzen. *Ann. Phys.*, 219(6):272–282, 1871.

[42] A. M. W. Tam, G. Qi, A. K. Srivastava, X. Q. Wang, F. Fan, V. G. Chigrinov, and H. S. Kwok. Enhanced performance configuration for fast-switching deformed helix ferroelectric liquid crystal continuous tunable lyot filter. *Applied Optics*, 53(17):3787–3795, Jun 2014.

[43] T. Uchida, K. Sato, and S. Inokuchi. An optical see-through mr display with digital micro-mirror device. *Trans. of the Virtual Reality Society of Japan*, 7(2), 2002. (in Japanese).

[44] T. Ueda, D. Iwai, T. Hiraki, and K. Sato. Illuminated focus: Vision augmentation using spatial defocusing via focal sweep eyeglasses and High-Speed projector. *IEEE Transaction on Visualization and Computer Graphics*, 26(5):2051–2061, May 2020.

[45] I. Šolc. Birefringent chain filters. *Journal of the Optical Society of America*, 55(6):621–625, Jun 1965.

[46] A. A. Wagadarikar, N. P. Pitsianis, X. Sun, and D. J. Brady. Video rate spectral imaging using a coded aperture snapshot spectral imager. *Opt. Express*, 17(8):6368–6388, Apr. 2009.

[47] A. Wilson and H. Hua. Design and demonstration of a vari-focal optical see-through head-mounted display using freeform alvarez lenses. *Optics*

Express, 27(11):15627–15637, 2019.

[48] A. Wilson and H. Hua. Design of a pupil-matched occlusion-capable optical see-through wearable display. *IEEE Transaction on Visualization and Computer Graphics*, 28(12):4113–4126, 2022.

[49] Y. Xu, A. Giljum, and K. F. Kelly. A hyperspectral projector for simultaneous 3d spatial and hyperspectral imaging via structured illumination. *Optics Express*, 28(20):29740–29755, Sep 2020.

[50] G. Yang, Z. Zheng, H. Li, and X. Liu. Method to reduce sidelobes of multistage lyot filters. *Applied Optics*, 49(8):1280–1287, Mar 2010.

[51] P. Yeh, A. Yariv, and C.-S. Hong. Electromagnetic propagation in periodic stratified media. i. general theory. *Journal of the Optical Society of America*, 67(4):423–438, Apr 1977.

[52] J. Zhang, R. Su, Q. Fu, W. Ren, F. Heide, and Y. Nie. A survey on computational spectral reconstruction methods from RGB to hyperspectral imaging. *Scientific Reports*, 12(1):11905, July 2022.

[53] Y. Zhang, X. Hu, K. Kiyokawa, N. Isoyama, H. Uchiyama, and H. Hua. Realizing mutual occlusion in a wide field-of-view for optical see-through augmented reality displays based on a paired-ellipsoidal-mirror structure. *Optics Express*, 29(26):42751–42761, Dec 2021.

[54] Y. Zhang, X. Hu, K. Kiyokawa, and X. Yang. Add-on occlusion: Turning Off-the-Shelf optical see-through head-mounted displays occlusion-capable. *IEEE Transaction on Visualization and Computer Graphics*, 29(5):2700–2709, 2023.